Deciphering spatial domains from spatially resolved transcriptomics with adaptive graph attention auto-encoder

Kangning Dong[1,2] and Shihua Zhang[1,2,3,4*]

[1]NCMIS, CEMS, RCSDS, Academy of Mathematics and Systems Science, Chinese Academy of Sciences, Beijing 100190, China;
[2]School of Mathematical Sciences, University of Chinese Academy of Sciences, Beijing 100049, China;
[3]Center for Excellence in Animal Evolution and Genetics, Chinese Academy of Sciences, Kunming 650223, China;
[4]Key Laboratory of Systems Biology, Hangzhou Institute for Advanced Study, University of Chinese Academy of Sciences, Chinese Academy of Sciences, Hangzhou 310024, China.

*To whom correspondence should be addressed. Tel/Fax: +86 01 82541360; Email: zsh@amss.ac.cn.

ABSTRACT

Recent advances in spatially resolved transcriptomics have enabled comprehensive measurements of gene expression patterns while retaining spatial context of tissue microenvironment. Deciphering the spatial context of spots in a tissue needs to use their spatial information carefully. To this end, we developed a graph attention auto-encoder framework STGATE to accurately identify spatial domains by learning low-dimensional latent embeddings via integrating spatial information and gene expression profiles. To better characterize the spatial similarity at the boundary of spatial domains, STGATE adopts an attention mechanism to adaptively learn the similarity of neighboring spots, and an optional cell type-aware module through integrating the pre-clustering of gene expressions. We validated STGATE on diverse spatial transcriptomics datasets generated by different platforms with different spatial resolutions. STGATE could substantially improve the identification accuracy of spatial domains, and denoise the data while preserving spatial expression patterns. Importantly, STGATE could be extended to multiple consecutive sections for reducing batch effects between sections and extracting 3D expression domains from the reconstructed 3D tissue effectively.

Introduction

The functions of complex tissues are fundamentally related to the spatial context of different cell types [1]. The relative locations of transcriptional expressions in a tissue is critical for understanding its biological functions and describing interactive biological networks [2]. Breakthrough technologies for spatially resolved transcriptomics (STs), such as 10x Visium [3], Slide-seq [4, 5] and Stereo-seq [6], have enabled genome-wide profiling of gene expressions in captured locations (referred to as spots) at a resolution of several cells or even subcellular levels.

Deciphering spatial domains (i.e., regions with similar spatial expression patterns) is one of the great challenges from STs. Most existing clustering methods do not efficiently use the available spatial information. These non-spatial methods can be roughly divided into two categories. The first category uses traditional clustering methods such as k-means and Louvain algorithm [7]. These methods are limited to the small number of spots or the sparsity according to the different resolutions of ST technologies, and clustering results may be discontinuous in the tissue section. The second category utilizes the cell type signatures defined by single-cell RNA-seq to deconvolute the spots [8, 9]. While these integration methods are appealing, as the spatial resolution improving, it is not applicable to technologies at a resolution of cellular or subcellular levels.

Some recent algorithms adapt the clustering methods by considering the similarity between adjacent spots to better account for spatial dependency of gene expressions [10-13]. These methods show significant improvements at identifying spatial domains of sections from brain and cancer tissues. For example, BayesSpace is a Bayesian statistical method that encourages neighboring spots to belong to the same cluster by introducing spatial neighbor structure into the prior [10]. stLearn defines the morphological distance based on features extracted from histology image, and utilizes such distances as well as spatial neighbor structure to smooth gene expressions [11]. SpaGCN combines spatial distances and histological information to construct a weighted graph of similarity between neighboring spots and employs a graph convolutional network to identify spatial domains [12]. SEDR employs a deep auto-encoder network for learning gene representations, and uses a variational graph auto-encoder to simultaneously embed spatial information [13]. Although these methods consider the spatial structure of STs, the similarity of neighboring spots defined by them is pre-defined before training and cannot be learned adaptively. Moreover, these methods do not consider the spatial similarity of spots at the boundary of spatial domains in more detail, and do not well integrate spatial information to impute and denoise gene expressions. More importantly, these approaches cannot be applied to multiple consecutive sections to reconstruct a three-dimensional (3D) ST model and extract 3D expression domains.

To this end, we developed a graph attention auto- encoder framework STGATE to accurately identify spatial domains by learning low-dimensional latent embeddings via integrating spatial information and gene expression profiles. Extensive tests and comparison with existing methods on ST data generated by different platforms (e.g., 10x Visium, Slide-seq and Stereo-seq) as benchmarks demonstrated its superiorities

for downstream analysis tasks such as spatial domain identification, visualization, spatial trajectory inference, data imputation and denoising, and 3D expression domain extraction.

Results

Overview of STGATE

STGATE starts by constructing the spatial neighbor network (SNN) based on the spatial locations, and optionally introduces the cell type-aware SNN by pruning the SNN based on the pre-clustering of gene expressions **(Fig. 1)**. Because the result of gene expression pre-clustering can effectively identify regions containing distinct cell types, this cell type-aware SNN can help to better characterize the spatial similarity at the boundary of these distinct spatial domains for ST data with low spatial resolutions, such as 10x Visium **(Materials and Methods)**.

Then STGATE learns low-dimensional latent embeddings with both spatial information and gene expressions via a graph attention auto-encoder [14] **(Fig. 1)**. The normalized expression of each spot is first transformed into a *d*-dimensional latent embeddings by an encoder, and then reversed them back into a reconstructed expression profile via a decoder. Differ from classic auto-encoder, STGATE adopts an attention mechanism in the middle layer of the encoder and decoder, which adaptively learns the edge weights of SNNs and further uses them to update the spot representation by collectively aggregating information from its neighbors. Finally, the latent embeddings are used to visualize with UMAP [15], and identify spatial domains with various clustering algorithms, such as mclust [16] and Louvain [7] **(Fig. 1).**

STGATE improves the identification of known layers on human dorsolateral prefrontal cortex dataset.

To quantitatively evaluate the spatial clustering performance of STGATE, we first applied it onto a 10x Visium dataset containing spatial expressions of 12 human dorsolateral prefrontal cortex (DLPFC) sections [17]. Maynard et al. [17] has manually annotated DLPFC layers and white matter (WM) based on the morphological features and gene markers **(Fig. 2a)**. Considering it as the ground truth, we compared the clustering accuracy of STGATE with three widely used clustering methods for single-cell RNA-seq analysis (k-means, Louvain [7] and mclust [16]), two recently developed spatial clustering approaches (BayesSpace [10] and stLearn [11]) and the unsupervised clustering assignments originally reported in the *spatialLIBD* package [17] in terms of adjusted rand index (ARI).

STGATE could effectively identify the expected cortical layer structures and achieve significant improvement compared to other six methods **(Fig. 2b, c and Supplementary Fig. S1)**. For example, in the DLPFC section 151676, STGATE clearly delineated the layer borders and achieved the best clustering accuracy (ARI=0.605) **(Fig. 2b)**. For comparison, the clustering assignment of non-spatial approach mclust also roughly followed the expected layer pattern in this section (ARI=0.468), but the boundary of its clusters was discontinuous with many outliers, which impaired its clustering accuracy. Moreover, STGATE also achieved the overall

best performance on all 12 sections of the DLPFC dataset **(Fig. 2c)**. Interestingly, the performance of algorithms leveraging the spatial information (stLearn, BayesSpace and STGATE) are generally better than the non-spatial clustering methods. These results demonstrated the superiority of STGATE at spatial domain identification and the necessity of its usage of spatial information.

The integration of spatial information enables STGATE to reveal the distance between spatial domains and depict the spatial trajectory in a UMAP plot [15]. For example, in the DLPFC section 151676, cortical layers were well-organized and showed consistent spatial trajectories (from layer 1 to layer 6 and white matter) in the UMAP plots generated by the STGATE embeddings **(Fig. 2d)**. This result is consistent with the function similarity between adjacent cortical layers as well as the chronological order [18]. By contrast, in the UMAP plots of PCA embeddings, spots belonging to distinct layers were not clearly separated, and spots of layer 1 were close to those of layer 6. We further confirmed the inferred trajectory using a trajectory inference algorithm named PAGA [19]. The PAGA graphs of STGATE embeddings on all the 12 DLPFC sections showed a nearly linear development trajectory from layer 1 to layer 6 as well as the similarity between adjacent layers, while the PAGA results of PCA embeddings were mixed **(Supplementary Fig. S2)**.

STGATE enables the identification of tissue structures from ST data of different spatial resolutions.

We further tested whether STGATE can be applied to ST data of different spatial resolutions. We applied STGATE onto a Slide-seqV2 dataset with 10μm spatial resolution from mouse hippocampus [5]. Compared to 10x Visium platform with a resolution of several cells per spot, Slide-seqV2 can profile spatial expressions at a resolution of cellular levels with more spots (>10,000 per section) but less sequence depth per spot **(Supplementary Table S1)**. As expected, STGATE can well characterize the tissue structures and uncover the spatial domains, while the clusters identified by PCA embeddings lack of clear spatial separation **(Fig. 2e, f and Supplementary Fig. S3)**. For example, STGATE depicted a clear “cord-like” structure as well as an “arrow-like” structure in the hippocampal region, and identified four spatial domains of it. This result is consistent with the annotation of hippocampus structures from the Allen Reference Atlas [20] **(Fig. 2g)**. Specifically, the “cord-like” structure corresponds to pyramidal layer of Ammon's horn, which can be further separated into fields CA1, CA2 and CA3 (i.e., CA1sp, CA2sp and CA3sp), and the “arrow-like” structure corresponds to the granule cell layer of dentate gyrus (i.e., DG-sg). Furthermore, the expressions of many known gene markers also verified the cluster partition of STGATE **(Supplementary Fig. S4)**. For example, ITPKA and BCL11B showed differential expressions between domains of Ammon's horn and are highly expressed at CA1sp as expected [21, 22]. The known molecular markers of hippocampal CA2sp such as PCP4 and AMIGO2 were specifically expressed in the identified CA2sp domain [23]. In addition, LRRTM4 that has been found to mediate excitatory synapse development on dentate gyrus granule cells, was specifically expressed at the identified DE-sg region [24]. Besides these known

tissue structures, STGATE also identified many well separated spatial domains and revealed their spatial gene expression patterns via differential expression analysis **(Supplementary Fig. S4)**. For example, the domain surrounding the hippocampal region (domain 2) expressed many oligodendrocytes-related gene markers such as TRF and MOBP [25]. The domain within the hippocampus except the “cord-like” and “arrow-like” structures (domain 3) exhibited strong expression of astrocytes gene markers DDN and CAMK2A [26]. Moreover, we also observed significant spatial expression patterns in the spatial domains 5 and 6 with the dominant expression of NWD2 and ENPP2 respectively. These results demonstrated that STGATE can dissect the spatial heterogeneity and further uncover spatial expression patterns. We also tested STGATE on the mouse hippocampus section profiled by Slide-seq and 10x Visium technologies. As the initial version of Slide-seqV2, the transcript detection sensitivity of Slide-seq is relatively lower [4] **(Fig. 2h)**. STGATE depicted the known tissue structures well except CA2sp on the Slide-seq data **(Fig. 2i)** and 10x Visium data **(Fig. 2j)** respectively.

We also validated the performance of STGATE for identifying tissue structures on mouse olfactory bulb, a widely used model tissue with laminar organization. We first tested STGATE on a ST dataset generated by Stereo-seq from mouse olfactory bulb tissues [6]. Stereo-seq is a newly emerging spatial omics technology that can achieve the subcellular spatial resolution by DNA nanoball patterned array chips. The data used here were binned into a resolution of cellular levels (~10μm) [6]. Fu et al. [13] has annotated the laminar organization of coronal mouse olfactory bulb in the DAPI-stained image, containing the rostral migratory stream (RMS), granule cell layer (GCL), internal plexiform layer (IPL), mitral cell layer (MCL), external plexiform layer (EPL) and olfactory nerve layer (ONL) **(Fig. 3a)**. Compared to the clusters produced by PCA embeddings, those identified using STGATE embeddings better reflected the laminar organization and well corresponded to the annotated layers **(Fig. 3b, c and Supplementary Fig. S5)**. Importantly, STGATE clearly recognized the narrow tissue structure MCL **(**the brown domain in **Fig. 3b)** and GL **(**the red domain in **Fig. 3b)**, while the results of PCA were mixed.

We also applied STGATE onto a mouse olfactory bulb section profiled by Slide-seqV2 [5], and found that the spatial domains identified by STGATE were well consistent with the annotation of coronal mouse olfactory bulb from Allen Reference Atlas [20] **(Fig. 3d)**. Specifically, compared to PCA, STGATE identified two spatial domains corresponding to accessory olfactory bulb (AOB) and the granular layer of accessory olfactory bulb (AOBgr) respectively **(Fig. 3e, f and Supplementary Fig. S6)**. These spatial domains uncovered by STGATE were clearly supported by gene markers **(Fig. 3g)**. For example, FXYD6 showed strong expressions on the identified AOB domain, which is consistent with its immunohistochemistry experiment [27]. The granular cell marker ATP2B4 [28] showed strong expressions on the identified AOBgr domain. The narrow MCL structure with the dominant expression of mitral cell marker GABRA1 [29] was also identified by STGATE. Moreover, we found that STGATE delineated the spatial trajectory among mouse olfactory bulb (from AOBgr to RMS to ONL) in the UMAP plots as well as the PAGA graphs **(Supplementary Fig. S7)**.

Collectively, these results illustrated the ability of STGATE to identify tissue structures and reveal their organization from ST data of different spatial resolutions.

Attention mechanism and cell type-aware module help to better characterize the similarity between neighboring spots.

Next, we tested whether STGATE could provide insights into sections including more biologically complex tissues, such as the whole brain. We applied STGATE onto a 10x Visium dataset, which profiled the spatial expressions of a coronal mouse brain section **(Fig. 4a)**. We found that the clustering results based on PCA embeddings of gene expressions roughly divided the tissue structures containing different cell types, while lack of the identification of small spatial domains **(Fig. 4b and Supplementary Fig. S8)**. For example, the clustering assignment based on PCA embeddings failed to identify the “cord-like” structure Ammon's horn and the “arrow-like” structure dentate gyrus within hippocampus. The direct application of STGATE brought some improvements at spatial domain identification **(Fig. 4c)**. Specifically, in the hippocampal region, STGATE without cell type-aware module identified the Ammon's horn, but did not depict the dentate gyrus structure.

For ST data containing heterogeneous cell types with low spatial resolution, STGATE with the cell type-aware module could better learn the spatial similarity **(Fig. 1; Materials and Methods)**. Specifically, the pre-clustering process are based on the Louvain algorithm with a small resolution parameter (set as 0.2 by default) **(Supplementary Fig. S8b)**. As expected, the usage of cell type-aware module aided in the identification of spatial domains **(Fig. 4d)**. STGATE identified the Ammon's horn as well as the dentate gyrus structure in the hippocampus, and further depicted the spatial domains CA1 and CA3 of the Ammon's horn. Moreover, we found that the cell type-aware module also significantly improved the separation of tissue structures in the UMAP plot **(Fig. 4e)**.

We further evaluated whether the usage of attention mechanism indeed contributed to better characterizing the heterogeneous similarity between neighboring spots. We visualized the attention layer by arranging the nodes according to their spatial locations and coloring the edges by their weights, and found that using attention mechanism alone could delineate the boundaries of main tissue structures such as the cortex, hippocampus and midbrain **(Fig. 4f)**. Combining the attention mechanism and the cell type-aware module enhanced the delineation of structure boundaries, and further revealed the spatial similarity within small spatial domains **(Fig. 4g)**. For example, in the hippocampal region, STGATE adaptively learned the spatial similarity within the Ammon's horn as well as the dentate gyrus structure **(Fig. 4h)**. Collectively, these results indicated the importance of the attention mechanism and cell type-aware module for depicting the similarity between neighboring spots.

STGATE imputes and denoises gene expressions for better characterizing spatial expression patterns.

STGATE could impute and denoise gene expressions. We compared the imputation performance of STGATE with four widely used single-cell RNA-seq imputation

algorithms: MAGIC [30], DeepImpute [31], scVI [32] and DCA [33] in terms of Spearman correlation coefficients in terms of genes and Pearson correlation coefficients of the imputation values to the reference data. We collected publicly available ST data from the similar tissue to construct three datasets, and conducted downsampling experiments in each section **(Materials and Methods; Supplementary Table S1)**. Notably, STGATE achieved the overall best performance at the DLPFC dataset and the Hippocampus dataset, and ranked second only to DeepImpute in the MouseBrain dataset **(Fig. 5a, b)**. Furthermore, compared to other imputation methods designed for single-cell RNA-seq, the usage of spatial information enables STGATE to preserve the spatial expression patterns. STGATE significantly improved the Moran's I values of spatially variable genes identified by SPARK-X compared to other approaches, which indicated that STGATE enhanced their spatial expression signals **(Fig. 5c)**. We further calculated the z-score of the Moran's I value of the identified spatially variable genes, and found that STGATE and scVI are the two best methods for preserving spatial patterns **(Fig. 5d)**. Notably, DeepImpute ranked first in the MouseBrain dataset, which included seven sections from the whole mouse brain, but performed poorly in the other two datasets. This result indicated that the similarity based on expressions alone is not enough to perform accuracy imputation in the tissues with homogeneous cell types, such as the cortex and hippocampus. We also employed two examples to illustrate the ability of STGATE to preserve the spatial expression patterns. First, we visualized the raw expression and the imputed expression of KRT17 gene, which is enriched in cortical layer 6 [17], in the DLPFC section 151676 **(Fig. 2a and Fig. 5e)**. Only STGATE clearly revealed its spatial expression pattern. By contrast, MAGIC and DCA incorrectly imputed missing values in the white matter region, and scVI imputed those in both the layers 1 and 6. Moreover, the expression of OCIAD2 showed strong specific expressions in the "cord-like" structure of hippocampus in the raw data profiled by Slide-seqV2, and only STGATE maintained its differential expression **(Fig. 5f)**.

Furthermore, we adopted STGATE to reduce noises in the DLPFC dataset to better show the spatial pattern of genes. We compared the expressions of five layer-marker genes of the raw data to those denoised ones by STGATE in the DLPFC section 151676 **(Fig. 6a)**. As expected, the denoised ones by STGATE clearly exhibited the laminar enrichment of these layer-marker genes. For example, ATP2B4 gene showed differential expressions in the layers 2 and 6, which is consistent with previously reported results [17, 34]. We also validated the laminar enrichment showed by STGATE against publicly available in situ hybridization (ISH) data from the Allen Human Brain Atlas [20] **(Fig. 6b)**. Moreover, comparison of the raw expressions and the denoised ones by STGATE using violin plots demonstrated that STGATE enhanced the spatial patterns of layer-marker genes **(Fig. 6c, d)**. Notably, STGATE obtained similar performance on the DLPFC section 151507 **(Supplementary Fig. S9)**. Collectively, these results demonstrated the ability of STGATE to impute missing values, reduce noises and enhance spatial expression patterns.

The usage of 3D SNN leads to better extraction of 3D spatial patterns.
We applied STGATE onto a pseudo 3D ST data constructed by aligning the spots of the "cord-like" structure in seven hippocampus sections profiled by Slide-seq **(Fig. 7a, b; Supplementary Table S2)**. The clustering results generated using PCA embeddings were mixed **(Supplementary Fig. S10)**. STGATE could clearly identify the known tissue structures when adopting the 3D SNN, but failed to identify the CA2sp region with only the 2D SNN **(Fig. 7c, d)**. We verified the tissue structures identified based on STGATE by the known marker genes, including ITPKA [21], BCL11B [22], AMIGO2 [23] and LRRTM4 [24] **(Supplementary Fig. S11)**. Moreover, when using the 2D SNN, spots belonging to different sections tended to cluster under each section rather than by cell types **(Fig. 7e, f)**. Notably, when adopting the 3D SNN, the UMAP visualizations verified that spots grouped entirely by cell types **(Fig. 7f)**. These results illustrated that STGATE could help to reconstruct 3D tissue model and accurately extract 3D expression patterns by incorporating 3D spatial information.

Discussion

Accurate identification of spatial domains and further extraction of spatially expressed genes are essential for understanding the tissue organization and biological functions. Here, we developed a fast and user-friendly spatial domain identification method STGATE, which can by seamlessly integrated into the standard analysis workflow by taking the "anndata" object of *scanpy* package [35] as inputs. STGATE transforms spatial location information into SNNs, and further adopts a graph attention auto-encoder to integrate SNNs and expression profiles. We tested performance of STGATE on diverse ST data generated by different platforms with different spatial resolutions. We found that STGATE accurately revealed the laminar organization of DLPFC and mouse olfactory bulb. Moreover, STGATE clearly identified the known tissue structures of hippocampus, and uncovered spatial domains of it. We additionally demonstrated the ability of STGATE in expression imputation and denoising by downsampling experiments. Lastly, we illustrated the ability of STGATE to alleviate batch effects between consecutive sections and extract 3D expression domains in a pseudo 3D hippocampus model.

The success of STGATE is mainly attributed to the usage of graph attention mechanism for considering the spatial neighbor information. However, current STGATE focuses on the integration of expression profiles and spatial information, and does not leverage the histological images. Actually, existing methods taking histological images as inputs, such as stLearn, did not achieve good performance in our comparison. stLearn employs a pre-trained neural network to extract features from images, and further calculates the morphological distance by cosine distance. We believe this pre-defined approach does not take advantages of the flexibility of deep learning, and the attention mechanism can be extended to adaptively integrate the histological image features conveniently.

STGATE can handle ST data of diverse spatial resolutions. Generally, STGATE performs better for ST data of cellular or subcellular resolutions due to the high similarity between neighboring spots. For technologies with relatively low spatial resolution, we introduced the cell type-aware module to depict the heterogeneous spatial similarity. However, a potential limitation of STGATE is that the whole SNN needs be loaded to GPU memory during training, which obstacles its applications onto very massive dataset. We expect to improve its scalability by introducing a subgraph-based training strategy in future work. Another limitation of STGATE is that it treats neighboring spots from the same section the same as those belonging to different sections. Future work may employ heterogeneous networks to better depict 3D tissue models.

Moreover, STGATE enables detection of spatially variable genes within spatial domains. Existing spatially variable gene identification algorithms such SPARK-X [36] do not consider the spatial domain information, which makes it difficult to identify space-specifically expressed genes within small tissue structures. To illustrate it, we compared differential expressed genes of STGATE spatial domains with those of SPARK-X on the Slide-seqV2 dataset from mouse olfactory bulb tissue. Specifically, STGATE identified 959 domain-specific genes, and SPARK-X searched 2,479 spatially variable genes with FDR<0.01. We found that many genes identified by SPARK-X did not show significant differences between spatial domains **(Supplementary Fig. S12a)**. Furthermore, the spatial autocorrelations measured by Moran's I statistic were similar between the gene set identified by STGATE and the first 1,000 genes of SPARK-X **(Supplementary Fig. S12b)**. Actually, the gene sets identified by these two methods have a great overlap, but SPARK-X ignores some specific genes of small tissue structures **(Supplementary Fig. S12c)**. For example, the mitral cell marker GABRA1 show significant enrichment in the MCL domain **(Fig. 3d; FDR=1e-34)**, but SPARK-X did not identify its spatial pattern **(FDR =0.018)**. Moreover, the NEFH gene also showed a strong expression in MCL domain **(Supplementary Fig. S12d; FDR=1e-12)**, while SPARK-X ignores it **(FDR=1)**. We expect that STGATE can facilitate the identification of tissue organization and the discovery of corresponding gene markers.

With the increase of the scale of ST data, STGATE is expected to be applied to large-scale data. We recorded the running time spent on real datasets by STGATE **(Supplementary Fig. S13a)**. When dealing with the largest real dataset with more than 50k spots, STGATE only cost about 40 minutes. We also benchmarked the running time and memory usage of STGATE on simulated datasets of different scales where spots were arranged according to the location of 10x Visium chips. Numerical experiments showed that STGATE was fast and only took less than 40 minutes with about 4GB GPU memory usage for dealing with the dataset with 50k spots **(Supplementary Fig. S13b)**. However, the GPU memory usage is nearly linearly correlated to the number of spots, and may be a bottleneck restricting the application of STGATE to massive datasets **(Supplementary Fig. S13c)**. Future work is expected to improve the scalability of STGATE by introducing the subgraph-based training strategy.

Materials and Methods

Data description

We applied STGATE to ST datasets generated by different platforms including 10x Visium, Slide-seq, Slide-seqV2 and Stereo-seq (see **Supplementary Table S1** for details). We mainly described the three datasets used for imputation experiments here. The DLPFC dataset includes 12 human DLPFC sections sampled from three individuals experiments [17]. The number of spots ranges from 3,498 to 4,789 for each section, and the original authors have manually annotated the area of DLPFC layers and white matter (WM). The MouseBrain dataset includes seven publicly available ST data of the whole mouse brain from the 10x Genomics website. Each section contains approximately 3,000 spots. The Hippocampus dataset consists of three Slide-seqV2 data from the mouse hippocampus [5], and the number of spots ranges from 19,285 to 52,869 for each section.

Moreover, seven ST data profiled by Slide-seq were used to reconstruct the 3D hippocampus model [4] (**Supplementary Table S2**). To generate the 3D hippocampus model, we first extracted the "cord-like" structure and "arrow-like" structure based on the STGATE embeddings in the entire section. Then sections are aligned using the Iterative Closest Point algorithm [37] and manual fine-tuning.

We also downloaded publicly available In situ hybridization (ISH) images and the annotation atlas images from the Allen Brain Atlas website [20] (**Supplementary Table S3**).

Data preprocessing

In all datasets, we first removed spots outside the main tissue area. Then raw gene expressions were log-transformed and normalized according to library size using *scanpy* package [35]. Finally, the top 3,000 highly variable genes were selected as the inputs of STGATE.

Construction of SNN

To incorporate the similarity of neighboring spots of a given spot, STGATE converts the spatial information into an undirected neighbor network according to a pre-defined radius *r*. Let **A** be the adjacency matrix of the SNN, then $\mathbf{A}_{ij} = 1$ if and only if the Euclidean distance between spot *i* and spot *j* is less than *r* **(Fig. 1)**. Specifically, for 10x Visium data, we set the network to contain the six nearest neighbors for each spot. For other data, we empirically choose *r* so that each spot contains 6-15 neighbors on average. The statistics of the number of neighbors for all the experiments can be found in **Supplementary Fig. S14**. Self-loops are added for each spot.

Construction of cell type-aware SNN (optional)

For ST data with relatively low spatial resolution, STGATE adopts a cell type-aware module by pruning the SNN according to pre-clustering of gene expressions. Specifically, the pre-clustering of gene expressions is conducted by the Louvain algorithm with a small resolution value (set as 0.2 by default) on the PCA embeddings, and STGATE prunes the edge if the spots of it belongs to different clusters **(Fig. 1)**.

Graph attention auto-encoder

The graph attention auto-encoder consists of three parts: encoder, decoder and graph attention layer.

Encoder

The encoder in our architecture takes the normalized gene expressions as input and generates the spot embedding by collectively aggregating information from its neighbors. Let x_i be the normalized expressions of spot *i* and *L* be the number of layer of the encoder. By treating expression profiles as initial spot embeddings (i.e. $\mathbf{h}_i^{(0)} = \mathbf{x}_i, \forall i \in \{1, 2, \ldots, N\}$), the *k*-th ($k \in \{1, 2, .., L-1\}$) encoder layer generates the embedding of spot *i* in layer *k* as follows:

$$\mathbf{h}_i^{(k)} = \sum_{j \in S_i} \mathbf{att}_{ij}^{(k)} \sigma\left(\mathbf{W}_k \mathbf{h}_j^{(k-1)}\right),$$

where $\mathbf{W}_k$ is the trainable weight matrix, σ is the nonlinear activation function, S_i is the neighbor set of spot *i* in SNN (including spot *i* itself) and $\mathbf{att}_{ij}^{(k)}$ is the edge weight between spot *i* and spot *j* in the output of the *k*-th graph attention layer. The *L*-th encoder layer does not adopt the attention layer and is formulated as follows:

$$\mathbf{h}_i^{(L)} = \sigma\left(\mathbf{W}_L \mathbf{h}_i^{(L-1)}\right).$$

The output of encoder is considered as the final spot embedding.

Decoder

By contrast, the decoder reverses the latent embedding back into a reconstructed normalized expression profile. By treating the output of the encoder as the input of the decoder (i.e. $\mathbf{h}_i^{(L)} = \mathbf{h}_i^{(L)}$), the *k*-th ($k \in \{2, .., L-1, L\}$) decoder layer reconstructs the embedding of spot *i* in layer *k*-1 as follows:

$$\mathbf{h}_i^{(k-1)} = \sum_{j \in S_i} \mathbf{att}_{ij}^{(k-1)} \sigma\left(\mathbf{W}_k \mathbf{h}_j^{(k)}\right).$$

Similar to the encoder, the last layer of decoder is formulated as follows:

$$\mathbf{h}_i^{(0)} = \sigma\left(\mathbf{W}_1 \mathbf{h}_j^{(1)}\right).$$

The output of decoder is considered as the reconstructed normalized expressions. To avoid overfitting, STGATE sets $\mathbf{W}^{(k)} = \mathbf{W}^{(k)^T}$ and $\mathbf{att}^{(k)} = \mathbf{att}^{(k)}$ respectively.

Graph attention layer

To adaptively learn the similarity between neighboring spots, we employed a self-attention mechanism which has been widely used for graph neural networks [38]. We first described it in the context of using SNN alone. Briefly, the attention mechanism is a single-layer feedforward neural network with shared parameters among nodes, parametrized by a weight vector. In the *k*-th encoder layer, the edge weight from node

i to its neighbor node *j* is computed as follows:

$$e_{ij}^{(k)} = \mathrm{Sigmoid}\left(\mathbf{v}_s^{(k)^T}\sigma\left(\mathbf{W}_k\mathbf{h}_i^{(k-1)}\right) + \mathbf{v}_r^{(k)^T}\sigma\left(\mathbf{W}_k\mathbf{h}_j^{(k-1)}\right)\right),$$

where $\mathbf{v}_s^{(k)}$ and $\mathbf{v}_r^{(k)}$ are the trainable weight vectors, and Sigmoid represents the sigmoid activation function.

To make the spatial similarity weights comparable, we normalized them by a softmax function as follows:

$$att_{ij}^{(k)} = \frac{\exp\left(e_{ij}^{(k)}\right)}{\sum_{l\in\mathcal{S}_i}\exp\left(e_{ij}^{(k)}\right)}.$$

These learned weights are further used to update the latent embedding in the encoder and decoder.

In addition, when the cell type-aware module is used, STGATE adopts self-attention mechanism for the two types of SNNs respectively. Let $\mathbf{att}_{ij}^{spatial}$ and $\mathbf{att}_{ij}^{aware}$ represent the learned spatial similarity based on SNN and the cell type-aware SNN respectively (the layer symbol is omitted here), and the spatial similarity finally adopted is the linear addition of them (α=0.5 by default):

$$\mathbf{att}_{ij} = (1-\alpha)\mathbf{att}_{ij}^{\mathrm{spatial}} + \alpha\mathbf{att}_{ij}^{\mathrm{aware}}.$$

Loss function

The objective of STGATE is to minimize the reconstruction loss of normalized expressions as follows:

$$\sum_{i=1}^{N}\left\|\mathbf{x}_i - \mathbf{h}_i^0\right\|_2.$$

Overall architecture of STGATE

In all experiments, the encoder of STGATE is set as a two-layer neural network (512-30) with the graph attention layer, and the decoder is set as the same number of layers as encoder. Adam optimizer [39] is used to minimize the reconstruction loss with an initial learning rate of 1e-4. The weight decay is set as 1e-4. The activation function is set as exponential linear unit (ELU) [40]. The number of iterations is set as 500 by default, and 1,000 when using the cell type-aware module.

Clustering

We used different strategies to identify spatial domains based on STGATE embeddings. When the number of label is known, we employ the mclust clustering algorithm [16]. For data without prior information, we use the Louvain algorithm from the *scanpy* package [35]. The resolutions of Louvain algorithm are manually selected. For fairness, we also displayed the results of Louvain algorithm under different resolutions.

Identifying differentially expressed genes

We used "Wilcoxon" test implemented in *scanpy* package [35] to identify differentially expressed genes for each spatial domain with 1% FDR threshold (Benjamini-Hochberg adjustment).

Generating reference and downsampled datasets

For benchmarking imputation performance, we first selected highly expressed genes from the raw data of each section as reference expressions. We then performed synthetic downsampling simulation by randomly flip 30% non-zero entries of the reference to zeros. The specific criterion for gene filtering is to keep about 2,000 genes with the highest proportion of non-zero expressing cells. Imputation methods were implemented using default parameters on the raw data containing entire genes, and the measurements of imputation accuracy were calculated based on selected genes.

Measuring spatial autocorrelation using Moran's I statistic

The Moran's I statistic [41] is a measure of spatial autocorrelation measure, and can be used to rank genes by their spatially informative rank [42]. For each individual gene *i*, the Moran's I statistic is computed using the formula:

$$I = \frac{N}{S_0} \frac{\sum_{i=1}^{N} \sum_{j=1}^{N} w_{ij} \left(y_i - \bar{y} \right) \left(y_j - \bar{y} \right)}{\sum_{i=1}^{N} \left(y_i - \bar{y} \right)^2},$$

where y_i and y_j is the expression profiles of spot *i* and spot *j*, $\bar{y}$ is the mean expression of gene, *N* is the number of spots, w_{ij} is the distance weight between spot *i* and spot *j*, and S_0 is the sum of w_{ij}. Obviously, the Moran's I statistic is bounded between -1 (a chess board like pattern) to 1 (a clear spatial pattern). We used the implementation of *Seurat* package [43], and w_{ij} is set as 1/distance.

Identification of 3D spatial domains using STGATE.

All current ST technologies profile gene expression patterns in the context of 2D tissue sections, which limits the accurate depiction of 3D ST in the real world. A conventional solution is to reconstruct gene expressions in 3D space by stacking consecutive 2D sections [4, 44]. However, batch effect between sections hinders the extraction of 3D spatial patterns. Here, we introduced a 3D SNN by incorporating the 2D SNN of each section and the SNN between adjacent sections to alleviate the batch effect between consecutive sections **(Fig. 7a)**. The key idea of the usage of 3D SNN is that the biological differences between consecutive sections should be continuous, so we can enhance the similarity between adjacent sections to eliminate the discontinuous

independent technical noises.

Data availability

All data analyzed in this paper are available in raw form from their original authors. Specifically, the DLPFC dataset is accessible within the *spatialLIBD* package (http://spatial.libd.org/spatialLIBD). The MouseBrain dataset is collected from the 10x Genomics website (https://support.10xgenomics.com/spatial-gene-expression/datasets). Slide-seqV2 datasets are available at https://singlecell.broadinstitute.org/single_cell/study/SCP815/highly-sensitive-spatial-transcriptomics-at-near-cellular-resolution-with-slide-seqv2#study-summary. Slide-seq datasets are available at https://portals.broadinstitute.org/single_cell/study/slide-seq-study. The processed Stereo-seq data from mouse olfactory bulb tissue is accessible on https://github.com/JinmiaoChenLab/SEDR_analyses.

Acknowledgements

This work has been supported by the National Key Research and Development Program of China [2019YFA0709501]; the Strategic Priority Research Program of the Chinese Academy of Sciences (CAS) [XDPB17], the Key-Area Research and Development of Guangdong Province [2020B1111190001], the National Natural Science Foundation of China [61621003]; the National Ten Thousand Talent Program for Young Top-notch Talents, and the CAS Frontier Science Research Key Project for Top Young Scientist [QYZDB-SSW-SYS008].

Author contributions

Shihua Zhang conceived and supervised the project. Kangning Dong designed, implemented, and validated STGATE algorithm. Kangning Dong and Shihua Zhang wrote the manuscript. All authors read and approved the final manuscript.

Competing interests

The authors declare no competing interests.

Reference

1. Asp, M., J. Bergenstråhle, and J. Lundeberg, *Spatially resolved transcriptomes—next generation tools for tissue exploration.* BioEssays, 2020. **42**(10): p. 1900221.
2. Armingol, E., et al., *Deciphering cell–cell interactions and communication from gene expression.* Nature Reviews Genetics, 2021. **22**(2): p. 71-88.
3. Ji, A.L., et al., *Multimodal analysis of composition and spatial architecture in human squamous cell carcinoma.* Cell, 2020. **182**(2): p. 497-514. e22.
4. Rodriques, S.G., et al., *Slide-seq: A scalable technology for measuring genome-wide expression at high spatial resolution.* Science, 2019. **363**(6434): p. 1463-1467.
5. Stickels, R.R., et al., *Highly sensitive spatial transcriptomics at near-cellular resolution with Slide-seqV2.* Nature biotechnology, 2021. **39**(3): p. 313-319.
6. Chen, A., et al., *Large field of view-spatially resolved transcriptomics at nanoscale resolution.* bioRxiv, 2021.
7. Blondel, V.D., et al., *Fast unfolding of communities in large networks.* Journal of statistical mechanics: theory and experiment, 2008. **2008**(10): p. P10008.
8. Elosua-Bayes, M., et al., *SPOTlight: seeded NMF regression to deconvolute spatial transcriptomics spots with single-cell transcriptomes.* Nucleic acids research, 2021. **49**(9): p. e50-e50.
9. Cable, D.M., et al., *Robust decomposition of cell type mixtures in spatial transcriptomics.* Nature Biotechnology, 2021: p. 1-10.
10. Zhao, E., et al., *Spatial transcriptomics at subspot resolution with BayesSpace.* Nature Biotechnology, 2021: p. 1-10.
11. Pham, D., et al., *stLearn: integrating spatial location, tissue morphology and gene expression to find cell types, cell-cell interactions and spatial trajectories within undissociated tissues.* bioRxiv, 2020.
12. Hu, J., et al., *Integrating gene expression, spatial location and histology to identify spatial domains and spatially variable genes by graph convolutional network.* bioRxiv, 2020.
13. Chen, J., et al., *Unsupervised Spatially Embedded Deep Representation of Spatial Transcriptomics.* 2021.
14. Salehi, A. and H. Davulcu. *Graph Attention Auto-Encoders*. in *2020 IEEE 32nd International Conference on Tools with Artificial Intelligence (ICTAI)*. 2020. IEEE.
15. McInnes, L., J. Healy, and J. Melville, *Umap: Uniform manifold approximation and projection for dimension reduction.* arXiv preprint arXiv:1802.03426, 2018.
16. Fraley, C., et al., *mclust version 4 for R: normal mixture modeling for model-based clustering, classification, and density estimation*. 2012, Technical report.
17. Maynard, K.R., et al., *Transcriptome-scale spatial gene expression in the human dorsolateral prefrontal cortex.* Nature neuroscience, 2021. **24**(3): p. 425-436.
18. Gilmore, E.C. and K. Herrup, *Cortical development: layers of complexity.* Current Biology, 1997. **7**(4): p. R231-R234.
19. Wolf, F.A., et al., *PAGA: graph abstraction reconciles clustering with trajectory inference through a topology preserving map of single cells.* Genome biology, 2019. **20**(1): p. 1-9.
20. Sunkin, S.M., et al., *Allen Brain Atlas: an integrated spatio-temporal portal for*

exploring the central nervous system. Nucleic acids research, 2012. **41**(D1): p. D996-D1008.

21. Windhorst, S., K. Song, and A.F. Gazdar, *Inositol-1, 4, 5-trisphosphate 3-kinase-A (ITPKA) is frequently over-expressed and functions as an oncogene in several tumor types.* Biochemical pharmacology, 2017. **137**: p. 1-9.
22. Lennon, M.J., et al., *Bcl11b—A Critical Neurodevelopmental Transcription Factor—Roles in Health and Disease.* Frontiers in cellular neuroscience, 2017. **11**: p. 89.
23. Laeremans, A., et al., *AMIGO2 mRNA expression in hippocampal CA2 and CA3a.* Brain Structure and Function, 2013. **218**(1): p. 123-130.
24. Siddiqui, T.J., et al., *An LRRTM4-HSPG complex mediates excitatory synapse development on dentate gyrus granule cells.* Neuron, 2013. **79**(4): p. 680-695.
25. Schäfer, I., et al., *MOBP levels are regulated by Fyn kinase and affect the morphological differentiation of oligodendrocytes.* Journal of cell science, 2016. **129**(5): p. 930-942.
26. Jouroukhin, Y., et al., *DISC1 regulates lactate metabolism in astrocytes: implications for psychiatric disorders.* Translational psychiatry, 2018. **8**(1): p. 1-12.
27. Kadowaki, K., et al., *Phosphohippolin expression in the rat central nervous system.* Molecular brain research, 2004. **125**(1-2): p. 105-112.
28. Zacharias, D.A. and C. Kappen, *Developmental expression of the four plasma membrane calcium ATPase (Pmca) genes in the mouse.* Biochimica et Biophysica Acta (BBA)-General Subjects, 1999. **1428**(2-3): p. 397-405.
29. Mamoor, S., *The α1 subunit of the γ-aminobutyric acid receptor, Gabra1, is differentially expressed in the brains of patients with schizophrenia.* 2020.
30. Van Dijk, D., et al., *Recovering gene interactions from single-cell data using data diffusion.* Cell, 2018. **174**(3): p. 716-729. e27.
31. Arisdakessian, C., et al., *DeepImpute: an accurate, fast, and scalable deep neural network method to impute single-cell RNA-seq data.* Genome biology, 2019. **20**(1): p. 1-14.
32. Lopez, R., et al., *Deep generative modeling for single-cell transcriptomics.* Nature methods, 2018. **15**(12): p. 1053-1058.
33. Eraslan, G., et al., *Single-cell RNA-seq denoising using a deep count autoencoder.* Nature communications, 2019. **10**(1): p. 1-14.
34. Zeng, H., et al., *Large-scale cellular-resolution gene profiling in human neocortex reveals species-specific molecular signatures.* Cell, 2012. **149**(2): p. 483-496.
35. Wolf, F.A., P. Angerer, and F.J. Theis, *SCANPY: large-scale single-cell gene expression data analysis.* Genome biology, 2018. **19**(1): p. 1-5.
36. Zhu, J., S. Sun, and X. Zhou, *SPARK-X: non-parametric modeling enables scalable and robust detection of spatial expression patterns for large spatial transcriptomic studies.* Genome Biology, 2021. **22**(1): p. 1-25.
37. Besl, P.J. and N.D. McKay. *Method for registration of 3-D shapes*. in *Sensor fusion IV: control paradigms and data structures*. 1992. International Society for Optics and Photonics.
38. Veličković, P., et al., *Graph attention networks.* arXiv preprint arXiv:1710.10903, 2017.
39. Kingma, D.P. and J. Ba, *Adam: A method for stochastic optimization.* arXiv preprint

arXiv:1412.6980, 2014.

40. Clevert, D.-A., T. Unterthiner, and S. Hochreiter, *Fast and accurate deep network learning by exponential linear units (elus).* arXiv preprint arXiv:1511.07289, 2015.
41. Li, H., C.A. Calder, and N. Cressie, *Beyond Moran's I: testing for spatial dependence based on the spatial autoregressive model.* Geographical Analysis, 2007. **39**(4): p. 357-375.
42. Nitzan, M., et al., *Gene expression cartography.* Nature, 2019. **576**(7785): p. 132-137.
43. Stuart, T., et al., *Comprehensive integration of single-cell data.* Cell, 2019. **177**(7): p. 1888-1902. e21.
44. Ortiz, C., et al., *Molecular atlas of the adult mouse brain.* Science Advances, 2020. **6**(26): p. eabb3446.

Figure captions:

Figure 1. Overview of STGATE. STGATE first constructs a spatial neighbor network (SNN) based on a pre-defined radius, and another optional one by pruning it according to the pre-clustering of gene expressions to better characterize the spatial similarity at the boundary of spatial domains. STGATE further learns low-dimensional latent representations with both spatial information and gene expressions via a graph attention auto-encoder. The input of auto-encoder is the normalized expression matrix, and the graph attention layer is adopted in the middle of the encoder and decoder. The output of STGATE can be applied for identifying spatial domains, data imputation and denoising, and extracting 3D spatial domains.

Figure 2. STGATE identifies known tissue structures in the human dorsolateral prefrontal cortex (DLPFC) tissue and the mouse hippocampus tissue. a, Ground-truth segmentation of cortical layers and white matter (WM) in the DLPFC section 151676. **b**, Cluster assignments generated by k-means, mclust, BayesSpace and STGATE in the DLPFC section 151676. **c**, Boxplot of clustering accuracy in all 12 sections of the DLPFC dataset in terms of adjusted rand index (ARI) score for seven methods. **d**, UMAP visualizations of the PCA and STGATE embeddings respectively. **e** and **f**, Spatial domains generated by Louvain clustering with resolution=0.3 on the low-dimensional PCA (**e**) and STGATE (**f**) embeddings in the Slide-seqV2 hippocampus section. **g**, The annotation of hippocampus structures from the Allen Reference Atlas of an adult mouse brain. **h**, Number of total UMIs per spot in the mouse hippocampus sections generated by Slide-seq and Slide-seqV2 respectively. **i** and **j**, Spatial domains generated by STGATE on the hippocampus section profiled by Slide-seq (**i**) and 10x Visium (**j**) technologies respectively.

Figure 3. STGATE identifies the laminar organization in the mouse olfactory bulb tissue sections profiled by Stereo-seq and Slide-seqV2 respectively. a, Laminar organization of mouse olfactory bulb annotated in the DAPI-stained image generated by Stereo-seq. **b** and **c**, Spatial domains generated by Louvain clustering with resolution=1 on the low-dimensional STGATE (**b**) and PCA (**c**) embeddings in the Stereo-seq mouse olfactory bulb tissue section. **d**, Laminar organization of mouse olfactory bulb annotated by the Allen Reference Atlas. **e** and **f**, Spatial domains generated by Louvain clustering with resolution=0.5 on the low-dimensional STGATE (**e**) and PCA (**f**) embeddings in the Slide-seqV2 mouse olfactory bulb tissue section. **g**, Visualization of spatial domains identified by STGATE and the corresponding marker genes. Spatial domains were annotated by the laminar organization showed in the Allen Reference Atlas.

Figure 4. STGATE reveals spatial domains in adult mouse brain section profiled by 10x Visium. a, Immunofluorescent imaging of the tissue section stained with DAPI and Anti-NeuN. **b-d**, Spatial domains generated by Louvain clustering with resolution=1 on the low-dimensional embeddings of PCA (**b**), STGATE (**c**) and

STGATE with cell type-aware module (**d**) respectively. **e**, UMAP visualizations of the low-dimensional embeddings of PCA, STGATE and STGATE with cell type-aware module respectively. **f** and **g**, Visualizations of the attention layer of STGATE without (**f**) or with (**g**) cell type-aware module. The nodes of attention layer are arranged according to the spatial position of spots. The edges of attention layer are colored by corresponding weights. **h**, Zoomed-in views of immunofluorescent imaging of the hippocampus region and the visualization of attention layer in (**g**).

Figure 5. Evaluation of imputation efficiency by downsampling. a and **b**, Gene-wise Spearman correlation (**a**) and Pearson correlation (**b**) values of all downsampling pairs in each section of the DLPFC dataset (10x Visium platform, 12 sections), the MouseBrain dataset (10x Visium platform, seven sections) and the Hippocampus dataset (Slide-seqV2 platform, three sections). **c** and **d**, Moran's I values (**c**) and the normalized Moran's I values (**d**) of the first 100 spatially variable genes identified by SPARK-X in the observed/imputed matrix. The outliers in the boxplot of (**d**) are ignored. **e**, Visualizations of KRT17 in the raw and imputed data in the DLPFC section 151676 respectively. **f**, Visualizations of OCIAD2 in the raw and imputed data in Slide-seqV2 Hippocampus section respectively.

Figure 6. STGATE enhances the spatial patterns of layer-marker genes in the DLPFC dataset. a, Visualizations of five layer-marker genes in the DLPFC section 151676. **b**, In situ hybridization (ISH) images from visual cortex (ATP2B4, RASGRF2, NEFH and NTNG2) or temporal cortex (LAMP5) of adult human brain from the Allen Human Brain Atlas. **c**, Violin plots of the raw expression of layer-marker genes. **d**, Violin plots of the STGATE denoised expressions of layer-marker genes. The cortical layer corresponding to the layer-marker gene is marked with a red box.

Figure 7. STGATE can alleviate the batch effect between consecutive sections by incorporating a 3D spatial network. a, The 3D spatial network is a combination of the 2D spatial network within each section and the spatial network between consecutive sections. **b**, Visualization of the 3D hippocampal volume stacked by seven aligned consecutive sections profiled by Slide-seq. **c** and **d**, Cluster assignments generated by STGATE using the 2D spatial network (**c**) and the 3D spatial network (**d**) respectively. **e**, UMAP visualizations of the low-dimensional embeddings of STGATE using the 2D spatial network and the 3D spatial network respectively. **f**, UMAP visualizations colored by section IDs and split by the types of used spatial networks.

Figure 1

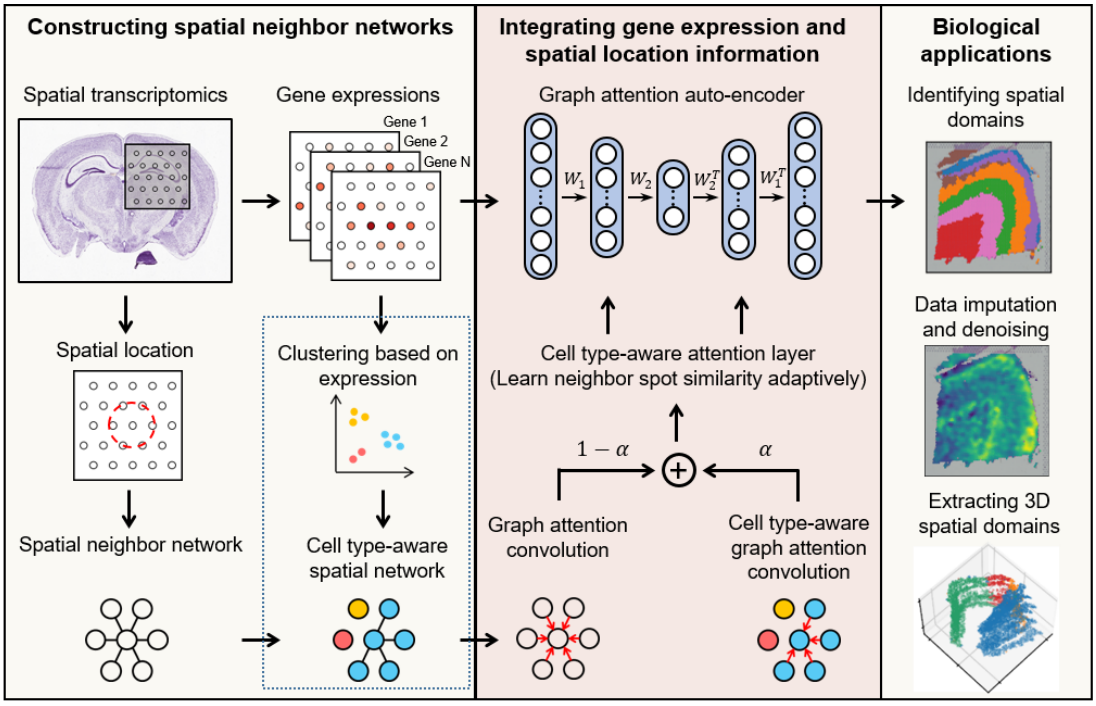
Constructing spatial neighbor networks
Integrating gene expression and spatial location information
Biological applications
Spatial transcriptomics
Gene expressions
Gene 1
Gene 2
Gene N
Graph attention auto-encoder
Identifying spatial domains
Spatial location
Clustering based on expression
Cell type-aware attention layer
(Learn neighbor spot similarity adaptively)
Data imputation and denoising
$1-\alpha$
α
Spatial neighbor network
Cell type-aware spatial network
Graph attention convolution
Cell type-aware graph attention convolution
Extracting 3D spatial domains

Figure 2

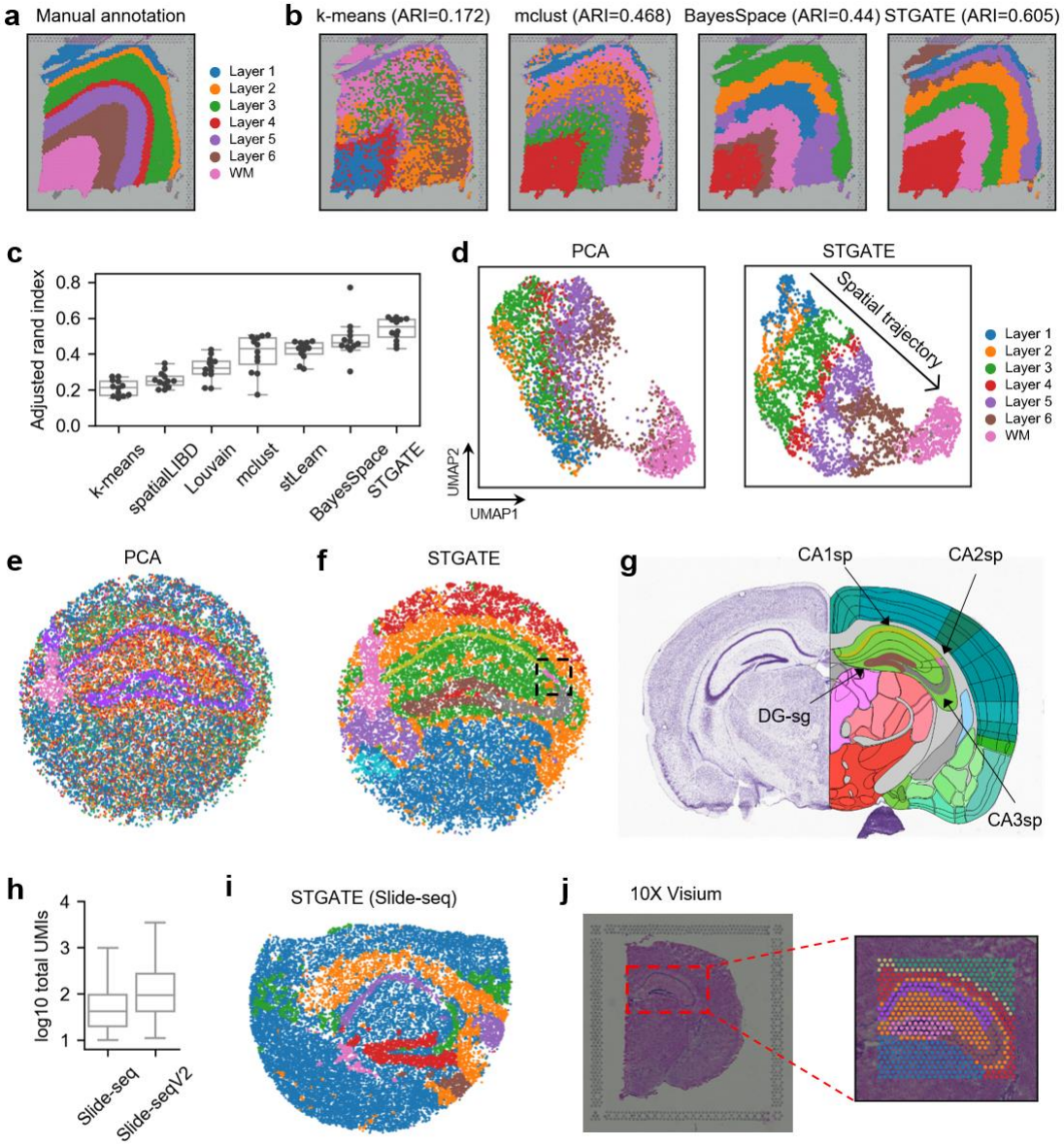
a
Manual annotation
Layer 1
Layer 2
Layer 3
Layer 4
Layer 5
Layer 6
WM
b
k-means (ARI=0.172)
mclust (ARI=0.468)
BayesSpace (ARI=0.44)
STGATE (ARI=0.605)
c
Adjusted rand index
0.0
0.2
0.4
0.6
0.8
k-means
spatialLIBD
Louvain
mclust
stLearn
BayesSpace
STGATE
d
PCA
STGATE
Spatial trajectory
UMAP2
UMAP1
Layer 1
Layer 2
Layer 3
Layer 4
Layer 5
Layer 6
WM
e
PCA
f
STGATE
g
CA1sp
CA2sp
DG-sg
CA3sp
h
log10 total UMIs
1
2
3
4
Slide-seq
Slide-seqV2
i
STGATE (Slide-seq)
j
10X Visium

Figure 3

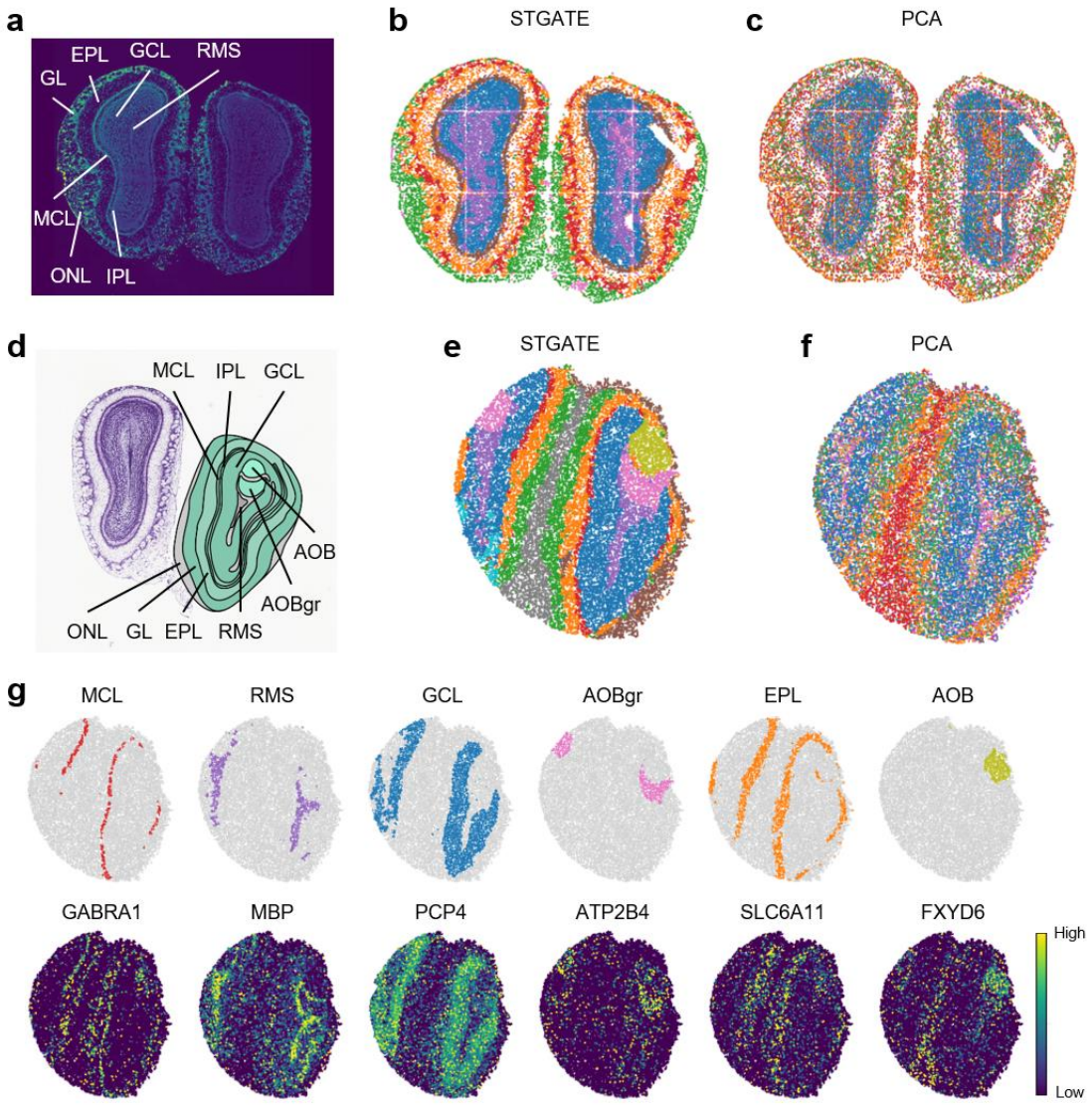
a
EPL
GCL
RMS
GL
MCL
ONL
IPL
b
STGATE
c
PCA
d
MCL
IPL
GCL
AOB
AOBgr
ONL
GL
EPL
RMS
e
STGATE
f
PCA
g
MCL
RMS
GCL
AOBgr
EPL
AOB
GABRA1
MBP
PCP4
ATP2B4
SLC6A11
FXYD6
High
Low

Figure 4

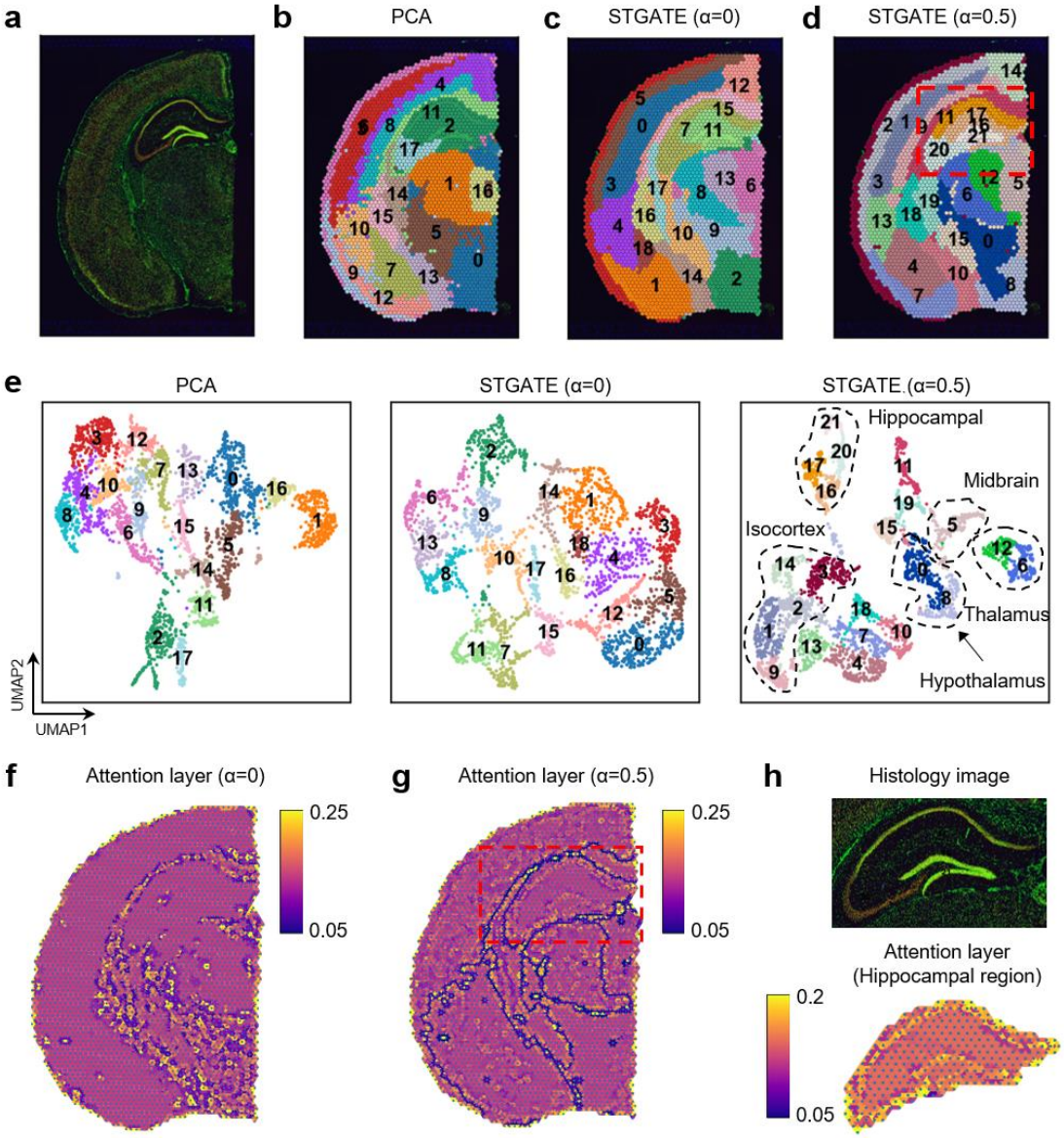
a
b
PCA
c
STGATE (α=0)
d
STGATE (α=0.5)
e
PCA
STGATE (α=0)
STGATE (α=0.5)
Hippocampal
Midbrain
Isocortex
Thalamus
Hypothalamus
UMAP2
UMAP1
f
Attention layer (α=0)
0.25
0.05
g
Attention layer (α=0.5)
0.25
0.05
h
Histology image
Attention layer
(Hippocampal region)
0.2
0.05

Figure 5

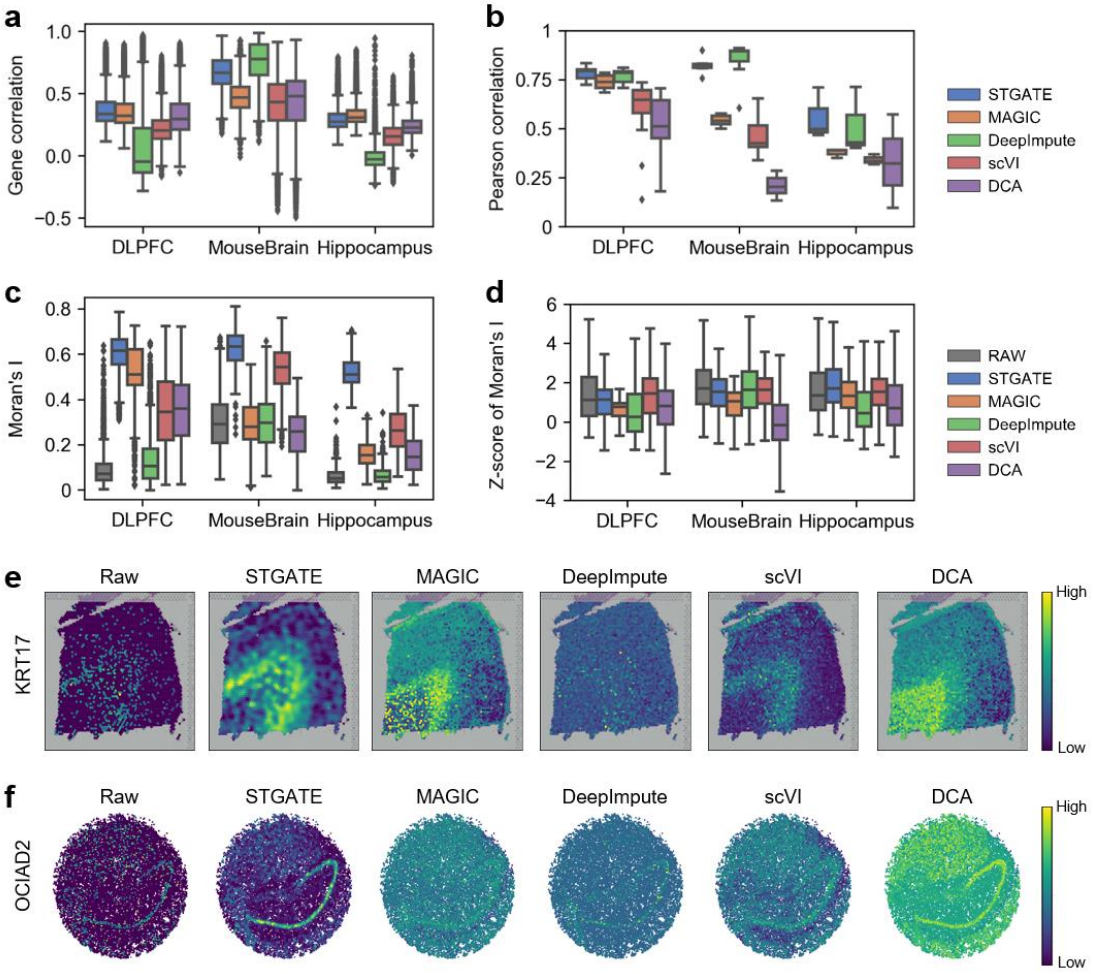
a
Gene correlation
1.0
0.5
0.0
−0.5
DLPFC
MouseBrain
Hippocampus
b
Pearson correlation
1
0.75
0.5
0.25
0
DLPFC
MouseBrain
Hippocampus
STGATE
MAGIC
DeepImpute
scVI
DCA
c
Moran's I
0.8
0.6
0.4
0.2
0
DLPFC
MouseBrain
Hippocampus
d
Z-score of Moran's I
6
4
2
0
−2
−4
DLPFC
MouseBrain
Hippocampus
RAW
STGATE
MAGIC
DeepImpute
scVI
DCA
e
KRT17
Raw
STGATE
MAGIC
DeepImpute
scVI
DCA
High
Low
f
OCIAD2
Raw
STGATE
MAGIC
DeepImpute
scVI
DCA
High
Low

Figure 6

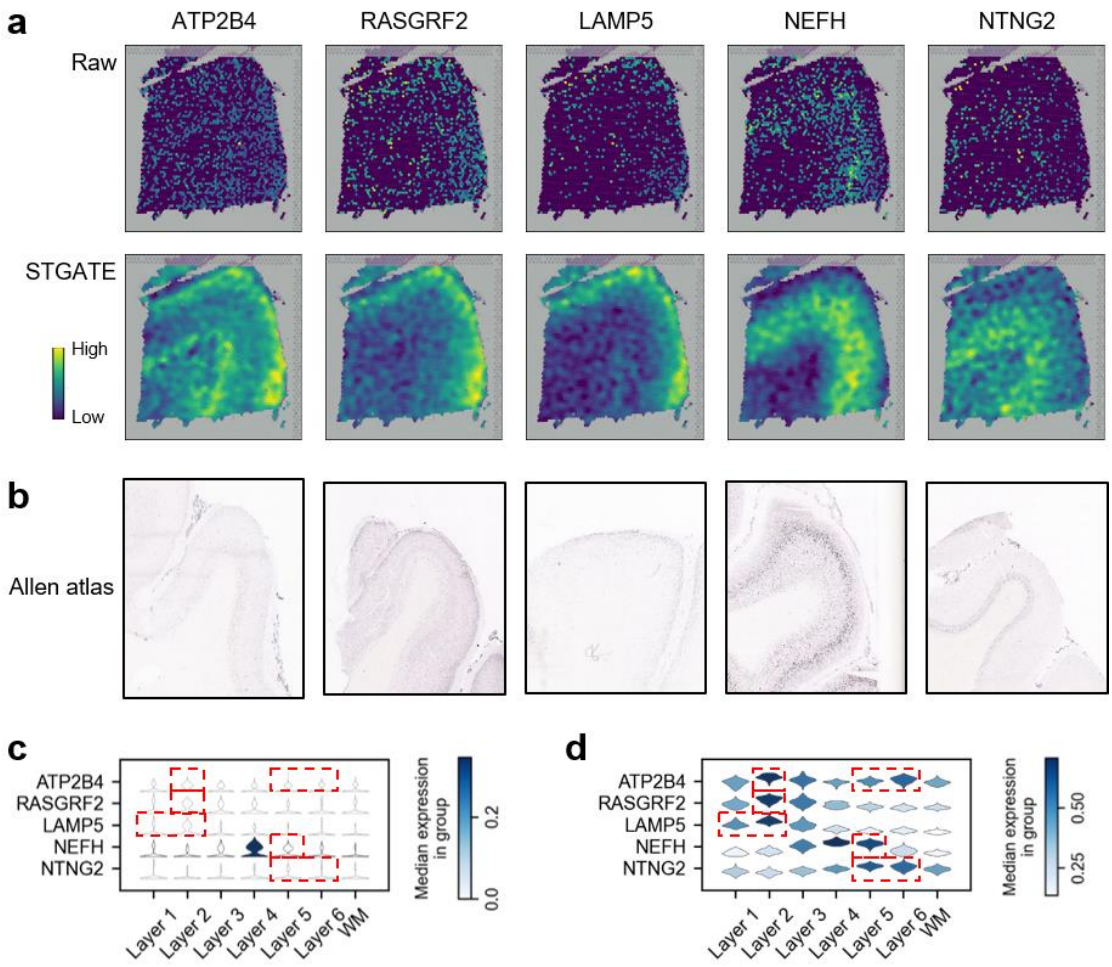
a
ATP2B4
RASGRF2
LAMP5
NEFH
NTNG2
Raw
STGATE
High
Low
b
Allen atlas
c
ATP2B4
RASGRF2
LAMP5
NEFH
NTNG2
Layer 1
Layer 2
Layer 3
Layer 4
Layer 5
Layer 6
WM
Median expression in group
0.0
0.2
d
ATP2B4
RASGRF2
LAMP5
NEFH
NTNG2
Layer 1
Layer 2
Layer 3
Layer 4
Layer 5
Layer 6
WM
Median expression in group
0.25
0.50

Figure 7

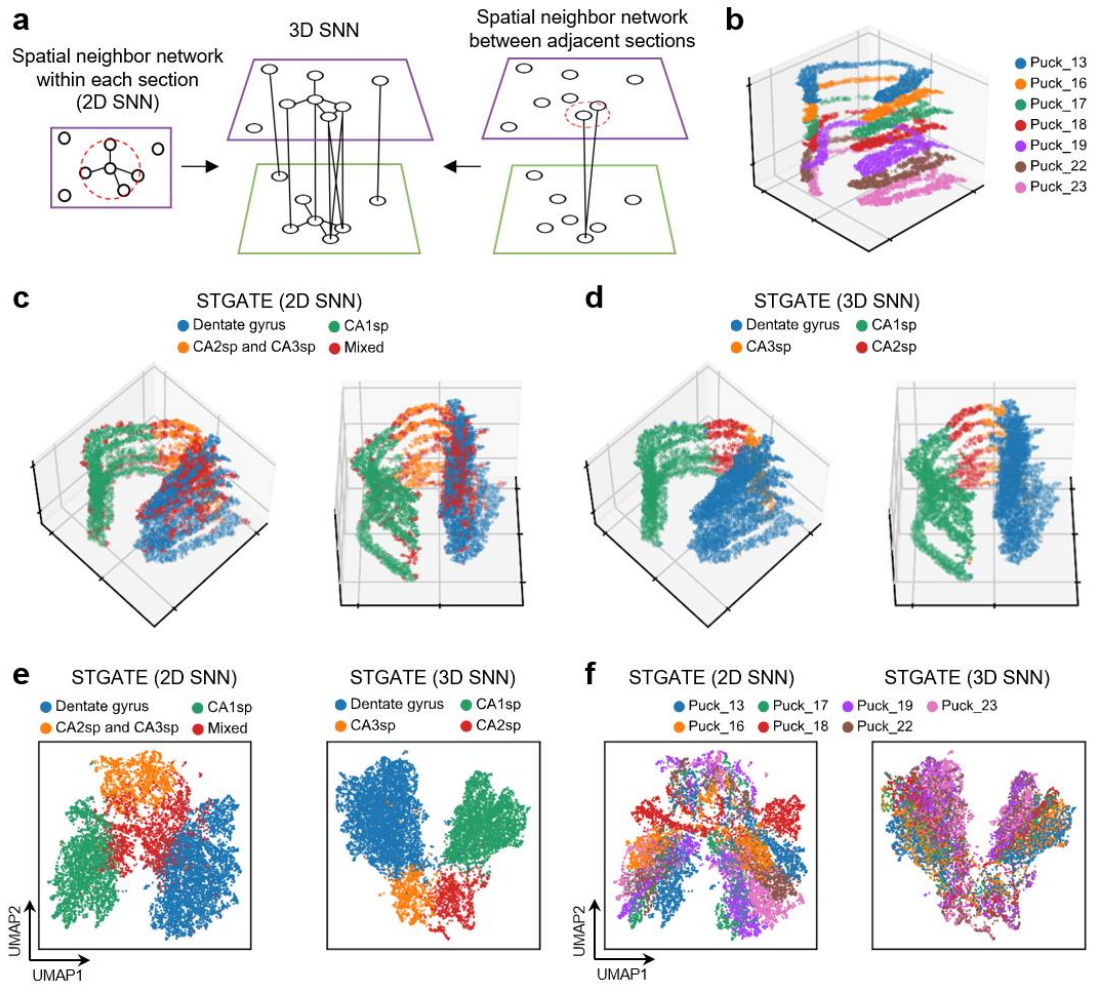
a
Spatial neighbor network within each section (2D SNN)
3D SNN
Spatial neighbor network between adjacent sections
b
Puck_13
Puck_16
Puck_17
Puck_18
Puck_19
Puck_22
Puck_23
c
STGATE (2D SNN)
Dentate gyrus
CA1sp
CA2sp and CA3sp
Mixed
d
STGATE (3D SNN)
Dentate gyrus
CA1sp
CA3sp
CA2sp
e
STGATE (2D SNN)
Dentate gyrus
CA1sp
CA2sp and CA3sp
Mixed
STGATE (3D SNN)
Dentate gyrus
CA1sp
CA3sp
CA2sp
UMAP2
UMAP1
f
STGATE (2D SNN)
STGATE (3D SNN)
Puck_13
Puck_17
Puck_19
Puck_23
Puck_16
Puck_18
Puck_22
UMAP2
UMAP1